Soft Matter

COMMUNICATION

View Article Online
View Journal | View Issue

Cite this: *Soft Matter*, 2021, **17**, 7252

Received 18th May 2021,
Accepted 15th July 2021

DOI: 10.1039/d1sm00738f

rsc.li/soft-matter-journal

Roughness-dependent clogging of particle suspensions flowing into a constriction†

Chiao-Peng Hsu, ‡*[a] Hasan Emre Baysal, §[a] Görel Wirenborn, [ab] Gustaf Mårtensson,[cd] Lisa Prahl Wittberg [b] and Lucio Isa *[a]

When concentrated particle suspensions flow into a constricting channel, the suspended particles may either smoothly flow through the constriction or jam and clog the channel. These clogging events are typically detrimental to technological processes, such as in the printing of dense pastes or in filtration, but can also be exploited in micro-separation applications. Many studies have to date focused on important parameters influencing the occurrence of clogs, such as flow velocity, particle concentration, and channel geometry. However, the investigation of the role played by the particle surface properties has surprisingly received little attention so far. Here, we study the effect of surface roughness on the clogging of suspensions of silica particles under pressure-driven flows along a microchannel presenting a constriction. We synthesize micron-sized particles with uniform surface chemistry and tunable roughness and determine the occurrence of clogging events as a function of velocity and volume fraction for a given surface topography. Our results show that there is a clear correlation between surface roughness and flow rate, indicating that rougher particles are more likely to jam at the constriction for slower flows. These findings identify surface roughness as an essential parameter to consider in the formulation of particulate suspensions for applications where clogging plays an important role.

1 Introduction

The flow of concentrated particle suspensions through microchannels is present in a broad range of technological applications, ranging from the ink-jet printing of solder paste or conductive adhesives for the microelectronics industry,[1,2] to drug delivery systems,[3,4] and 3D printing processes.[5,6] When suspensions flow through a narrow constriction, the particles may either flow continuously, intermittently, or permanently jam at the constriction depending on the suspension's volume fraction, channel geometry, and flow rates.[7–9] Such clogging events are encountered in different systems across various length scales, including crowds of people evacuating or escaping a room,[9,10] flocks of sheep entering a barn,[11] self-driving vehicles,[12] discharging of dry granular silos,[13] sand flowing through the neck of an hourglass,[14] and in microfluidic filtration.[15,16] Despite the apparent analogies among these systems, the underlying clogging mechanisms may be fundamentally different.

In the case of particulate suspensions, clogging is in general detrimental because it reduces the performance and lifetime of the equipment and devices,[17–19] and leads to uncontrolled behavior, such as self-filtration.[20] However, the spontaneous occurrence of clogging events can also be exploited to benefit specific processes, such as in micro-sieving systems[21] and for cancer cell separation.[22] In spite of a wealth of studies on the converging flow of dense suspensions, *i.e.*, examining the role of various key parameters, from the constriction's geometry to the type of fluid surrounding the particles,[23–30] the effect of particle surface topography, *i.e.*, surface roughness, has remained largely unexplored. However, it has recently been shown that surface roughness plays a critical role in determining the jamming volume fraction and the rheological response of dense suspensions subjected to high shear[31–34] under conditions closely resembling those under which clogging may occur. Considering that the particles used in applications often display irregular, rough surfaces and deviate from perfectly smooth spheres, elucidating the role played by surface roughness in clogging therefore constitutes a worthwhile endeavor.

In order to approach this problem in a systematic way, we explore the impact of surface roughness on the clogging of aqueous particulate suspensions by studying model silica colloids with tunable roughness in a converging microfluidic channel of

[a] *Laboratory for Soft Materials and Interfaces, Department of Materials, ETH Zürich, 8093 Zürich, Switzerland. E-mail: lucio.isa@mat.ethz.ch*
[b] *FLOW, Department of Engineering Mechanics, KTH, Stockholm, Sweden*
[c] *Division of Nanobiotechnology, Department of Protein Science, Science for Life Laboratory, KTH Royal Institute of Technology, Solna, Sweden, Sweden*
[d] *Mycronic AB, Täby, Sweden*

† Electronic supplementary information (ESI) available. See DOI: 10.1039/d1sm00738f

‡ Present address: Lehrstuhl für Biophysik (E27), Technische Universität München, D-85748 Garching, Germany. E-mail: chiao-peng.hsu@tum.de

§ Present address: Materials Engineering Department (MTM), KU Leuven, Leuven, Belgium.

fixed geometry. Comparing the clogging conditions of particles with different surfaces allows us to identify the contribution of interlocking among surface asperities as a primary factor in determining the occurrence of clogs.

2 Methods

2.1 Materials

Silica particles 50 nm (NanoXact Silica Nanospheres), 75 nm (NanoXact Silica Nanospheres), 100 nm (NanoXact Silica Nanospheres), 150 nm (Nanocym), 1.93 μm (microParticles), polydiallyldimethylammonium chloride solution (poly-DADMAC) (400–500 kDa, 20 wt% in water; Sigma-Aldrich), tetraethyl orthosilicate (TEOS; 98%; Sigma-Aldrich), ammonium hydroxide (NH_4OH) (25% in water; Sigma-Aldrich), hydrogen peroxide (H_2O_2) (30% in water; Merck Millipore), polydimethylsiloxane (PDMS) (SYLGARD 184 Silicone Elastomer Kit; DOW) were used as received.

2.2 Synthesis of raspberry-like silica particles

The synthesis of rough, raspberry-like particles with controlled surface topography was modified from a previous procedure.[35] In this work, 1.93 μm silica particles were used as the core particles and 50 nm, 75 nm, 100 nm, and 150 nm silica particles were used as the asperities. A cleaning process was performed in order to remove any possible organic compounds and activate the hydroxy groups on the surface of the core particles. 10 mL of 1.93 nm silica suspension (5 wt%) was added to a mixture containing 10 mL of NH_4OH and 10 mL of H_2O_2 at 70 °C under stirring at 500 rpm (Heidolph MR 2002) for 10 min. The cleaned particles were washed three times by centrifugation (376 rcf, 3 min), and the aqueous supernatant was exchanged with Milli-Q water. After the final wash, the cleaned core particles were dispersed in 50 mL of Milli-Q water, giving a 1 wt% suspension.

An aqueous mixture containing 40 mL of the cleaned core suspension (1 wt%) and 200 mL of poly-DADMAC (0.025 wt%) was stirred at 750 rpm for 60 min in order to obtain positively charged core particles. The core particles were then washed three times (376 rcf, 3 min), and the aqueous supernatant was exchanged with Milli-Q water to remove the excess of poly-DADMAC. After the final wash, the positively charged core particles were dispersed in 400 mL of Milli-Q water, giving a 0.1 wt% suspension. Afterwards, 100 mL of core particle suspension (0.1 wt%) was mixed with 12 mL of suspensions of silica nanoparticles (naturally displaying a negative charge) at 1 wt% under stirring at 750 rpm for 60 min. The electrostatically adsorbed nanoparticles constitute the surface asperities, where by changing the nanoparticle size, one controls the asperity dimensions. The obtained raspberry-like particles were washed three times by centrifugation (376 rcf, 3 min), and the aqueous supernatant was exchanged with Milli-Q water. After the final wash, the cleaned raspberry-like particles were dispersed in 10 mL of Milli-Q water, giving a 1 wt% suspension.

After these steps, the asperities were enclosed within an additional layer of silica to provide permanent mechanical bonding. In particular, TEOS molecules were used to grow a amorphous silica layer on the surface of the raspberry-like particles. A total of 37.7 mL ethanol, 6.2 mL NH_4OH and 5 mL 1 wt% raspberry-like particle suspension were mixed together. A 5 vol% of TEOS in ethanol solution was injected into the mixture by a syringe pump (NE-1000; New Era Pump Systems Inc.) with a rate of 2 mL h^{-1}. The TEOS solution was added in 4 cycles. Each cycle consisted of adding 0.267 mL of TEOS solution following by an additional 25 min break. The mixture was stirred at 500 rpm during the first cycle and ultra-sonicated during the last three cycles. The reaction temperature was kept constant by applying water cooling. The final raspberry-like particles were washed three times by centrifugation (376 rcf, 3 min), and the aqueous supernatant was exchanged with Milli-Q water. After the final wash, the cleaned raspberry-like particles were dispersed in 5 mL of Milli-Q water, giving a 1 wt% suspension.

2.3 Characterization of raspberry-like silica particles

Samples for scanning electron microscopy (SEM) (LEO 1530; Zeiss) were prepared by spreading 2 μL of particle suspensions (1 wt%) on UV/ozone-cleaned (ProCleaner PLUS; UVFAB) silicon wafers. The samples were sputter-coated (CUU-010; Safematic) with 3 nm of platinum to avoid surface charging prior to SEM imaging.

Atomic force microscopy (AFM) (NanoWizard NanoOptics; JPK Instruments AG) was used to record the surface topography and analyze surface roughness. The AFM samples were prepared by dropping and spreading 5 μL of a particle suspension on a UV/ozone-cleaned round glass slide.

The AFM data were analyzed in four steps using custom-written codes written in Mathematica (Wolfram Research) and MATLAB (R2018b, Mathworks). First, the center of each particle was identified by recognizing the local maximum of a band-pass-filtered image. Second, the radius of each particle was extracted by fitting its profile with a sphere. Third, the fitted spherical volume was subtracted from the AFM height image in order to obtain the genuine surface topography decoupled from the underlying curvature. In this way, we obtained a flattened particle surface. Finally, for the largest possible square inscribed in the scanned particle section, root-mean-square roughness (R_{RMS}) was used to describe and compare the surface roughness of the different raspberry-like particles. In addition, the average distance between asperities, d, and average asperity height, h, were extracted to model asperity interlocking and to compare R_{RMS} and h/d roughness.

2.4 Microfluidic channel design and production

The microfluidic channel used in our experiments consists of an inlet, an outlet, two sets of pillar filters, a pre-constriction channel, and the constriction channel as shown in Fig. 1a. The inlet and outlet are designed to fit standard tubing and then scaled down to the pre-constriction channel. A grid of pillar filters are placed inside the inlet and between the inlet and the pre-constriction channel to encourage monodisperse particle flows by filtering out unwanted agglomerates. From the pre-constriction channel to the constriction channel, the channel width is scaled down from 500 μm down to 24 μm with a 45° angle.

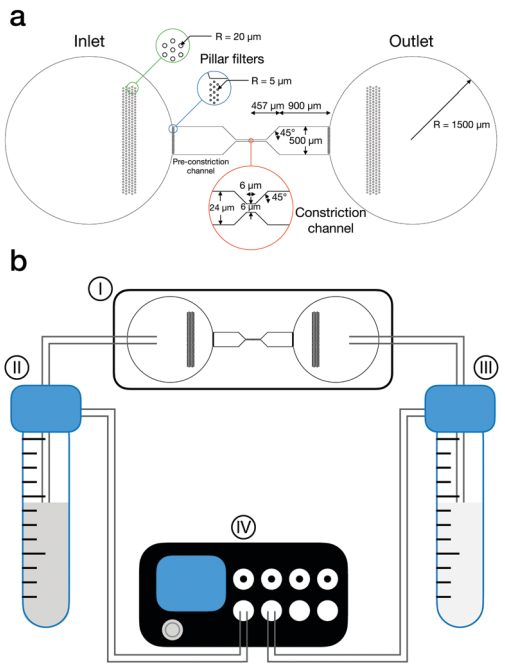

Fig. 1 Channel design and flow experiment. (a) Scaled drawing of the designed microfluidic channel, where the inlet, pillar filters, pre-constriction channel, constriction channel, and outlet are indicated. The green, blue, and red zoom-in show the details of the two pillar filters and constriction channel. (b) Schematic of the experimental setup: the microfluidic chip (I), the particle suspension reservoir (II), the Milli-Q reservoir (III), and the pressure-controlled pump (IV).

At the constriction, the width of the channel is narrowed from 24 μm down to 6 μm with a 45° angle. The ratio of channel width D to particles diameter $2r$ is designed that $D/2r \approx 3$, based on the observations that clogging is likely to occur when $D/2r \approx 3.4$, even with dilute suspensions.[3] For $D/2r > 3$, the flow becomes uninterrupted even for dramatic increases in volume fraction.[29] The channel height is 6 μm. The final design was realized using AutoCAD software (Autodesk).

The designed channel master was fabricated on a silicon wafer using photolithography. The positive chromium plate photomask was manufactured by Mycronic AB and the subsequent fabrication of the silicon master was performed by Ångströmlaboratoriet Uppsala at Uppsala University.

The microfluidic channel was fabricated by soft-lithography[36] using PDMS (SYLGARD 184 Silicone Elastomer Kit; DOW). The two components of the PDMS kit were poured in a container with a 10 : 1 polymer/curing agent ratio. This mixture was mixed at 2000 rpm for 1 min and degassed for 1 min (ARE-250; THINKY). The thoroughly mixed and degassed mixture was poured carefully on the channel master and left to cure for 24 h at 70 °C. Afterward, the cured PDMS was gently removed from the master and robustly rinsed with ethanol. Two holes were punctured at the inlet and outlet.

The final microfluidic chip was prepared by bonding the PDMS channel to a glass slide. This was done by treating the surfaces of the PDMS channel and of the glass slide for 2 min in an oxygen plasma cleaner (PDC-32G; Harrick Plasma). Prior to the plasma treatment, the glass slide was sonicated and rinsed with toluene, isopropanol, ethanol, and Milli-Q and dried with pressurized nitrogen.

2.5 Flow experiments

The microfluidic chip was mounted on a inverted microscope (Axio Observer; Zeiss or ECLIPSE Ti2; Nikon) and the flow experiments were recorded with a CMOS camera (Zyla 5.5; Oxford Instruments).

The flow inside the channel was driven by a pressure-controlled pump (MK3; ElveFlow) connecting the inlet and outlet of the channel to two reservoirs, one containing Milli-Q water and one containing the particle suspension at 0.1 wt%, *via* PTFE tubing (1/16 inch outer diam., 1/32 inch inner diam.; ElveFlow), as shown in Fig. 1b. The microfluidic channel was initially flushed with Milli-Q to test the sealing of the channel before connecting the particle suspension reservoir. This check was performed by increasing the pressure in the Milli-Q reservoir (Fig. 1b, III) from 10 mbar to 200 mbar at a rate of 1 mbar s^{-1}. Afterwards, the particle suspension reservoir (Fig. 1b, II) was also connected to the tubing and pressurized from 10 mbar to 200 mbar at a rate of 1 mbar s^{-1} to fill the microfluidic chip with the particles. Both pressures were kept at 200 mbar until no further air bubbles were left in the channel and both pressures were decreased to 20 mbar steadily with a rate of 1 mbar s^{-1}. The pressure in the particle suspension reservoir was gently increased until flowing particles were observed in the channel. At this stage, in order to increase the concentration of the particles in the region of interest, the microfluidic chip was inclined by $\approx 5°$. Thereafter, the particles were allowed to accumulate in the constriction region to reach the desired initial volume fraction. This process required 1 h to 12 h. After the particles were concentrated in the constriction region, the incline was removed. The flow from reservoir II to III was then gradually reduced by increasing the pressure in the Milli-Q reservoir until an optimum pressure at which the particles stayed stationary. The particle flow through the constriction channel was driven back and forth every 15 s by superimposing an additional pressure difference between the particle suspension and Milli-Q reservoir ranging between 0.2 and 5 mbar.

During the back-and-forth cycles, the magnitude of the pressure difference remained constant. This operation mode allowed us to break clogs occurring in one direction, restart the experiments in a standardized way and reuse the same suspension in the channel over long time windows. Each flow period was thus treated as an independent experiment, with constant applied pressure, during which we measured the flow velocity and the volume fraction upstream of the constriction. The volume fraction and, correspondingly, the flow varied between different runs depending on flow history, *e.g.*, clog or no-clog. Screening multiple runs thus enabled us to scan through a broad range conditions in a single, closed experiment.

2.6 Image analysis

Image sequences were acquired at 20 fps over 5 min during the flow experiments. Spatiotemporal diagrams were used to

visualize and identify the occurrence of clogging events during an image sequence. These diagrams were constructed by extracting a single-pixel horizontal line through the middle of the constriction channel from each image and stacking them vertically as a function of time.

The particle volume fraction (ϕ) and mean velocity ($\bar{v}$) for which a clogging event occurred were calculated from the upstream area (19.6 μm × 19.6 μm) next to the constriction channel (Fig. 3a). ϕ was obtained by $\phi = (N_{particle} \times V_{particle})/V_{channel}$. The number of particles $N_{particle}$ was identified by a MATLAB code. The upper bound of the volume of particle $V_{particle\_max}$ was calculated based on the maximum diameter measured in SEM images and the lower bound of the volume of particle $V_{particle\_interlock}$ was calculated based on the effective interlocked particle size (see Fig. S1, ESI†). The volume of the selected channel $V_{channel}$ was 19.6 × 19.6 × 6 μm^3. $\bar{v}$ was obtained from the frame before each clogging event using the particle image velocimetry (PIV) tool (PIVlab)[37] in MATLAB, dividing each frame in a 10 × 10 matrix.

3 Results and discussion

The starting point of the experiments is the synthesis of a range of raspberry-like silica particles with tailored roughness. The surface roughness, diameters, particle volume ratios, and neck-to-particle ratios of the smooth silica particle and four different raspberry-like silica particles are summarized in Table 1. Smooth silica particles are named SM and raspberry-like silica particles are named RB_R_{RMS}, where R_{RMS} is the value of the root-mean-squared roughness parameter of the silica surface measured by AFM as described in the Methods. Fig. 2 displays the different silica particles employed in this study. R_{RMS} can be used to compare roughness between the particles investigated due to having the same core particle, *i.e.*, a similar diameter, and all asperities having a spherical cap morphology. The surface roughness of the model particles was tuned by using differently sized nanoparticles so that the bigger the size of the nanoparticles used, the higher the measured R_{RMS}. In these conditions, the R_{RMS} roughness is interchangeable with the quantification of roughness based on asperity distance and height (h/d values) as used in previous studies[33] (see Fig. S2, ESI†). The five particle systems are charge-stabilized ($\zeta \approx -50$ mV in 1 mM aqueous KCl solution) and have the same surface chemistry due to their pristine silica surface. The uniform surface chemistry allows us to focus on the influence of surface roughness on the clogging events, disregarding variations in colloidal interactions.

During an experiment, flow can either proceed uninterrupted (Fig. 3a) or a clogging event can take place at the constriction (Fig. 3b). In the case of clogging, the constriction is obstructed by a small number of particles in contact held together by the friction among them. The pressure difference is maintained causing the suspending medium to continue flowing and displacing the particles downstream of the clog, while an accumulation of particles is observed upstream from the clog. The spatio-temporal diagram of a flow experiment without any clogging shows a zigzag pattern, reflecting the change of the flow direction every 15 s (Fig. 3c – left). The flow velocities were estimated by measuring the slope of the zigzag pattern, where 1/slope corresponds to the mean flow velocity in the middle of the constriction channel. In case of clogging events, discontinuities can directly be seen in the spatiotemporal diagram (Fig. 3c – right). The blank area downstream of the constriction indicates that no further particles flow through the clog and the vertical lines accumulating upstream of the constriction indicate that here the particles are immobile and that the clog front moves in the direction opposite to the flow direction. Upon reversing the flow direction, the clogs are usually removed and flow of the suspension starts in the opposite direction (see Movie S1, ESI†).

Table 1 Surface roughness (R_{RMS}), diameter ($2r$), particle volume ratio ($V_{particle\_max}/V_{particle\_interlock}$), and neck-to-particle ratio ($D/2r$) of the particles

	SM	RB_10	RB_14	RB_21	RB_30
R_{RMS} (nm)	0.8 ± 0.2	10 ± 2	14 ± 2	21 ± 6	30 ± 6
$2r$ (μm)	1.98 ± 0.03	2.08 ± 0.06	2.18 ± 0.06	2.21 ± 0.05	2.29 ± 0.06
$V_{particle\_max}/V_{particle\_interlock}$	1	1.095	1.219	1.133	1.119
$D/2r$	3.03 ± 0.05	2.97 ± 0.09	2.94 ± 0.08	2.83 ± 0.06	2.72 ± 0.07

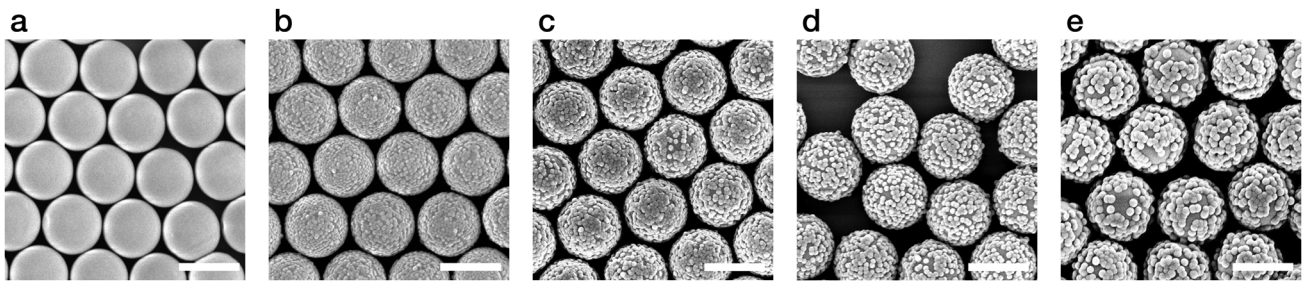

Fig. 2 Smooth and rough silica particles. Scanning electron microscopic images of SM (a), RB_10 (b), RB_14 (c), RB_21 (d), and RB_30 (e). Scale bars indicate 2 μm.

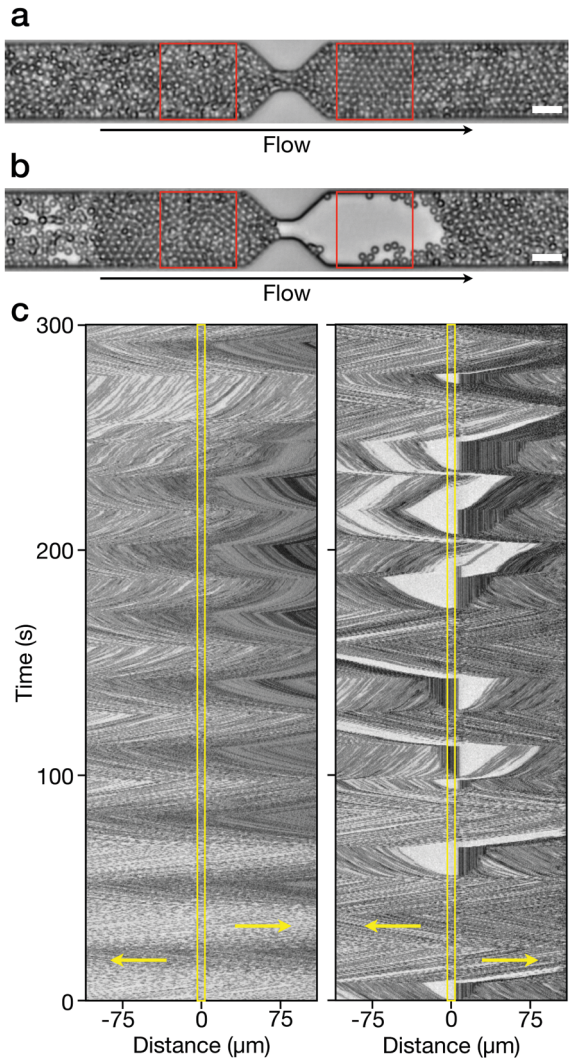

Fig. 3 Flow experiments in the constriction channel. (a) RB_30 particles flow in the constriction channel without clogging. Flow direction is from left to right. (b) RB_30 particles clog at the constriction channel. Flow direction is from left to right. The red squares in a and b mark the area for the calculations of particle volume fraction (ϕ) and mean velocity ($\bar{v}$). Scale bars indicate 10 μm. (c) Spatiotemporal diagrams of no clogging (left, SM particles) and multiple clogging events (right, RB_30 particles) across the constriction channel. The yellow rectangles mark the position of the constriction and the yellow arrows indicate the flow direction.

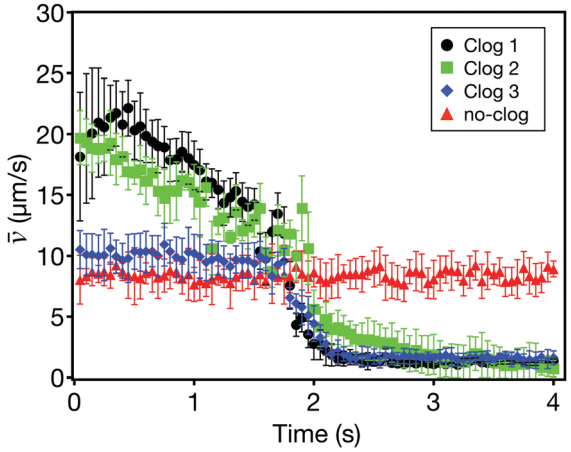

Fig. 4 Temporal evolution of the mean velocity. Time evolution of the mean velocity ($\bar{v}$) of clogging (●, ■, ♦; clog at t = 2 s) and non-clogging flows (▲) for RB_30. Error bars represent the standard deviations of the velocity extracted from PIV measurements dividing each frame in a 10 × 10 matrix.

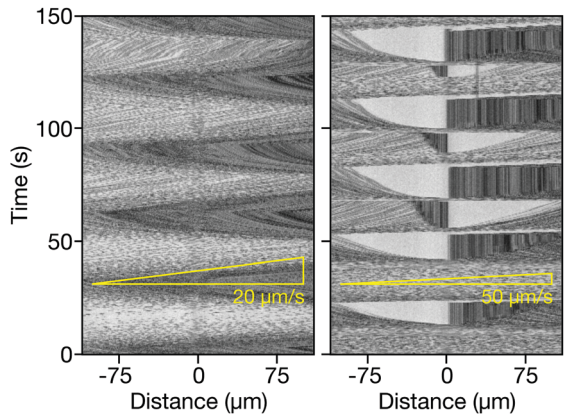

Fig. 5 Clogging events of SM suspensions. Spatiotemporal diagrams of SM particles flowing slower than 30 μm s^{-1} (left) displaying a continuous flow and SM particles flowing faster than 50 μm s^{-1} (right) displaying clogging events. The inset shows slopes corresponding to 20 μm s^{-1} and 50 μm s^{-1}.

In order to avoid any spurious results, experimental data where clogs are generated by small particle agglomerates that have not been properly filtered out and by defects in the fabrication of the constriction channel were removed. For all experimental data sets, the particle volume fraction (ϕ) and mean flow velocity ($\bar{v}$) were measured immediately preceding a clogging event, as described in the Methods. The occurrence of clogs can be clearly identified by plotting the time evolution of $\bar{v}$ of different clogging events (Fig. 4 and Fig. S3, ESI†).

In general, we find that the occurrence of clogs is a function of both ϕ and $\bar{v}$ for any given surface roughness. For instance, we do not observe any clogging events in the SM suspensions at the typical flow velocity range (up to 30 μm s^{-1}) in our flow experiments (see Movie S2, ESI†). However, we notice that clogging events can happen for the SM suspensions when the flow velocity is higher than 50 μm s^{-1} (Fig. 5 and Movie S3, ESI†). This velocity-dependent clogging implies that there is a characteristic timescale for the formation of a clog relative to a rearrangement timescale, allowing incoming particles to flow through the constriction channel without obstructing it.

However, we find that the likelihood for a clog to form strongly depends on the particle surface roughness. In particular, compared to the SM suspensions, the RB suspensions clog at much slower flow velocities, suggesting that surface topography hinders particle rearrangements as they enter the constriction. We attribute this difference to the distinctive ways in which smooth and rough particles interact at close contact. In the occurrence of the breakage of lubricating fluid film at high shear, particles enter in boundary-lubricated contacts,[38,39]

determined by their effective solid–solid friction coefficient. Here, relative motion among smooth particles is possible by sliding against each other, and the increased dissipation due to sliding friction slows rearrangements down. However, the surface asperities on the RB particles can interlock, preventing any sliding and giving rise to much longer-lived flow-induced structures.

By collecting data over multiple experiments as a function of ϕ and $\bar{v}$ for the SM and RB suspensions, we can identify the occurrence of clogs as shown in Fig. 6a. Here, each data point corresponds to a clogging event taking place for a given $(\bar{v}, \phi)$ pair. The scattering of individual clogging events of each suspension emphasizes the stochastic nature of the phenomenon. However, while the clogs happen indistinctly across a ϕ range from 0.1 to 0.2 for all the suspensions, the scatter plot shows the emergence of clearer correlation between $\bar{v}$ and surface roughness. We therefore plot the averaged $\bar{v}$ of each suspension for all ϕ against the R_{RMS} of the particles as shown in Fig. 6b. From the averaged data, it is evident that particles with higher surface roughness tend to clog at a lower $\bar{v}$. Remarkably, for the same volume fraction range, the critical speed for clogging sees a fourteen-fold decrease from the SM particles to the roughest RB ones, from $\bar{v} \approx 70$ μm s^{-1} to $\bar{v} \approx 5$ μm s^{-1}. As previously reported, clogging is strongly affected by the neck-to-particle ratio. However, for our particle systems, the difference in this ratio between SM and RB_30 is 10% (Table 1), which is within the experimental error of other systems showing a clear dependence of neck-to-particle ratio on clogging.[17,29,30] Moreover a significant difference in the onset of clogging is already seen between the SM and the RM_10, where this difference is as small as 2%. This strongly indicates that surface roughness plays a crucial role.

In order to quantify the effect of roughness more clearly, we replot the data in Fig. 6b to include the effect of volume fraction and flow velocity in a single quantity, also accounting for the differences in neck-to-particle ratio among the different particles. To this end, we report the average number flow rate of particles entering the constriction $\dot{N}$. This quantity represents the number of particles flowing through the constriction per unit time necessary to induce, on average, a clog, and is defined as:

$$\dot{N} = \frac{N_{\text{particle}} \cdot \bar{v} \cdot A_{\text{particle}}}{V_{\text{channel}}} \quad (1)$$

This definition considers the variations of the neck-to-particle ratio, because we use a value of A_{particle} which includes the possibility of particle interlocking across the constriction. The data clearly show a strong dependence of $\dot{N}$ on RMS roughness as shown in Fig. 6c, even if the values of $D/2r$ are all within 10%.

The results presented in Fig. 6c therefore define an indicative phase diagram, identifying a roughness-dependent flow rate below which the suspension does not clog in our experiments and above which clogging is observed. The deeper one enters the clogging regime, the higher is the likelihood for a clog to happen, *i.e.* for the roughest particles, the suspensions almost immediately clogs at flow velocities above a few microns per second, for volume fractions above 10%. Additional analysis has been performed for dense granular systems in a quasistatic regime, where it has been shown that spatial and temporal fluctuations in the interparticle forces and velocities can be used as a characteristic to identify how close/far a system is from the boundary between flowing/non-flowing regimes.[40–43] Conversely, our experiments take place in an intermediate regime, where identifying a clear description of the stress fluctuations and their correlation with flow characteristics becomes experimentally very challenging. However, our findings indicate that the interlocking of the asperities hinders particle rearrangements at the constriction, leading to the appearance of force networks at lower flow rates for rougher systems, in line with what has been reported for discontinuously shear-thickening systems and shear-jamming suspensions. The extension of our study to the case of quasi-static granular systems with controlled surface roughness

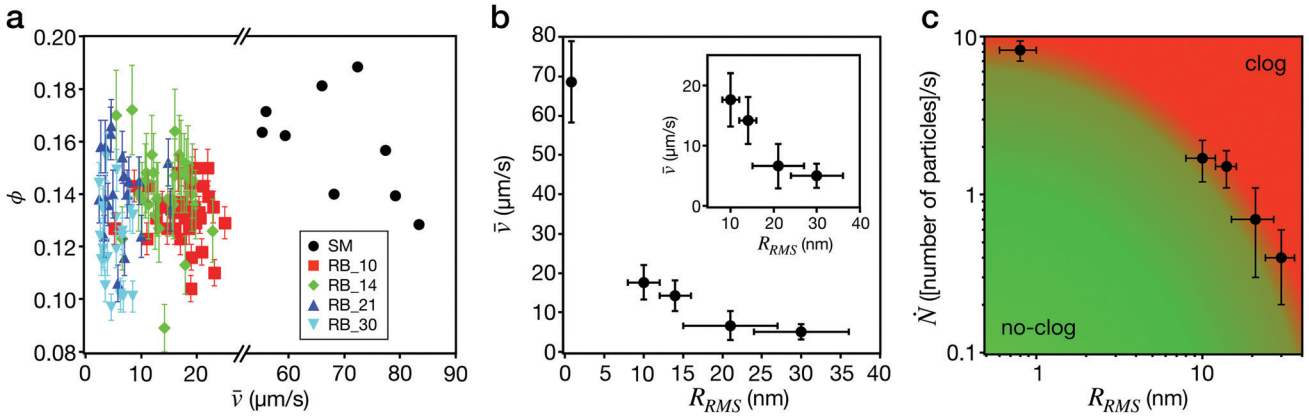

Fig. 6 Roughness-dependent clogging events. (a) Volume fraction (ϕ) and mean velocity ($\bar{v}$) in correspondence of each clogging event for SM (●), RB_10 (■), RB_14 (♦), RB_20 (▲), and RB_30 (▼). Error bars in ϕ represent the upper and lower bounds of volume fractions estimated by the maximum particle size and the effective particle size after interlocking, respectively. (b) Average flow velocity $\bar{v}$ preceding a clogging event as a function of particle surface roughness (R_{RMS}). The inset shows only the RB particles. Error bars in $\bar{v}$ represent the standard deviations from all clogging events in a. Error bars in R_{RMS} represent the standard deviations from AFM roughness measurements. (c) Dependence of $\dot{N}$ on R_{RMS}. The red area marks the clogging regime and the green area marks the non-clogging regime.

would be highly beneficial to elucidate the role of topography interlocking on the stress distribution among particles under flow.

4 Conclusions

This data indicates that roughness has a dramatic impact on the clogging of particle suspensions entering constriction flows and should be considered comprehensively when engineering the suspensions flow behavior. The correlation between $\dot{N}$ and R_{RMS} leading to clogging events, in particular, provides evidence that boundary contacts providing asperity-interlocking events strongly restrict relative motion among particles with a clear impact on high-shear flows, as amply reported for rheometric flows. This conclusion offers an alternative approach to prevent or delay clogging, orthogonal to nozzle design. The strategy hinges on engineering the tribology of contacts, whenever possible by tailoring surface topography. In the case in which the morphology of the particles cannot be controlled *a priori*, this approach still offers opportunities to promote particle rearrangements by coating them with low-friction polymers layers[44,45] or by engineering the composition of the suspension.[33,34] The latter path can strongly reduce the formation of flow-induced, stress-bearing structures by adding a small fraction of particles of different size or different surface roughness and therefore reduce the propensity to clog. We expect that the results obtained with our model particles will prompt the adoption of this approach for systems of applied relevance.

Author contributions

Author contributions are defined based on the CRediT (Contributor Roles Taxonomy) and listed alphabetically. Conceptualization: CPH, LI, GM. Formal analysis: HEB, CPH, GL. Funding acquisition: LI, GM. Investigation: HEB, CPH, GL. Methodology: HEB, CPH, LI, GL, GM, LPW. Project administration: LI, GM, LPW. Resources: GM. Supervision: CPH, LI, GM, LPW. Validation: HEB, CPH, GL. Visualization: CPH. Writing – original draft: CPH. Writing – review and editing: CPH, LI, GM, LPW.

Conflicts of interest

The authors declare no competing interests.

Acknowledgements

The authors thank Charles Björnberg and Ola Jacobsson (Mycronic AB) and Javier Cruz (Uppsala University) for their help with designing and manufacturing the channel mask and master and thank André Studart for access to the SEM. CPH and LI acknowledge the financial support of the ETH Research Grant ETH-49 16-1.

References

1 S. B. Fuller, E. J. Wilhelm and J. M. Jacobson, *J. Microelectromech. Syst.*, 2002, **11**, 54–60.
2 S. Y. Wu, C. Yang, W. Hsu and L. Lin, *Microsyst. Nanoeng.*, 2015, **1**, 15013.
3 K. V. Sharp and R. J. Adrian, *Microfluid. Nanofluid.*, 2005, **1**, 376–380.
4 C. Kleinstreuer, J. Li and J. Koo, *Int. J. Heat Mass Transfer*, 2008, **51**, 5590–5597.
5 D. Kokkinis, M. Schaffner and A. R. Studart, *Nat. Commun.*, 2015, **6**, 8643.
6 M. K. Hausmann, P. A. Rühs, G. Siqueira, J. Läuger, R. Libanori, T. Zimmermann and A. R. Studart, *ACS Nano*, 2018, **12**, 6926–6937.
7 L. Isa, R. Besseling, E. R. Weeks and W. C. K. Poon, *J. Phys.: Conf. Ser.*, 2006, **40**, 124–132.
8 L. Isa, R. Besseling, A. N. Morozov and W. C. K. Poon, *Phys. Rev. Lett.*, 2009, **102**, 058302.
9 I. Zuriguel, D. R. Parisi, R. C. Hidalgo, C. Lozano, A. Janda, P. A. Gago, J. P. Peralta, L. M. Ferrer, L. A. Pugnaloni, E. Clément, D. Maza, I. Pagonabarraga and A. Garcimartín, *Sci. Rep.*, 2014, **4**, 7324.
10 D. Helbing, I. Farkas and T. Vicsek, *Nature*, 2000, **407**, 487–490.
11 A. Garcimartín, J. M. Pastor, L. M. Ferrer, J. J. Ramos, C. Martín-Gómez and I. Zuriguel, *Phys. Rev. E: Stat., Nonlinear, Soft Matter Phys.*, 2015, **91**, 022808.
12 G. A. Patterson, P. I. Fierens, F. Sangiuliano Jimka, P. G. König, A. Garcimartín, I. Zuriguel, L. A. Pugnaloni and D. R. Parisi, *Phys. Rev. Lett.*, 2017, **119**, 248301.
13 I. Zuriguel, A. Garcimartín, D. Maza, L. A. Pugnaloni and J. M. Pastor, *Phys. Rev. E: Stat., Nonlinear, Soft Matter Phys.*, 2005, **71**, 051303.
14 X.-l. Wu, K. J. Måløy, A. Hansen, M. Ammi and D. Bideau, *Phys. Rev. Lett.*, 1993, **71**, 1363–1366.
15 J. Lin, D. Bourrier, M. Dilhan and P. Duru, *Phys. Fluids*, 2009, **21**, 073301.
16 P. Bacchin, A. Marty, P. Duru, M. Meireles and P. Aimar, *Adv. Colloid Interface Sci.*, 2011, **164**, 2–11.
17 H. M. Wyss, D. L. Blair, J. F. Morris, H. A. Stone and D. A. Weitz, *Phys. Rev. E: Stat., Nonlinear, Soft Matter Phys.*, 2006, **74**, 061402.
18 H. L. Leverenz, G. Tchobanoglous and J. L. Darby, *Water Res.*, 2009, **43**, 695–705.
19 M. Tavakkoli, M. R. Grimes, X. Liu, C. K. Garcia, S. C. Correa, Q. J. Cox and F. M. Vargas, *Energy Fuels*, 2015, **29**, 2890–2900.
20 M. D. Haw, *Phys. Rev. Lett.*, 2004, **92**, 185506.
21 G. Brans, J. Kromkamp, N. Pek, J. Gielen, J. Heck, C. van Rijn, R. van der Sman, C. Schroën and R. Boom, *J. Membr. Sci.*, 2006, **278**, 344–348.
22 L. Pang, S. Shen, C. Ma, T. Ma, R. Zhang, C. Tian, L. Zhao, W. Liu and J. Wang, *Analyst*, 2015, **140**, 7335–7346.
23 A. I. Campbell and M. D. Haw, *Soft Matter*, 2010, **6**, 4688–4693.
24 D. Genovese and J. Sprakel, *Soft Matter*, 2011, **7**, 3889–3896.

25 C. C. Thomas and D. J. Durian, *Phys. Rev. E: Stat., Nonlinear, Soft Matter Phys.*, 2013, **87**, 052201.
26 J. Koivisto, M. Korhonen, M. Alava, C. P. Ortiz, D. J. Durian and A. Puisto, *Soft Matter*, 2017, **13**, 7657–7664.
27 E. Dressaire and A. Sauret, *Soft Matter*, 2017, **13**, 37–48.
28 X. Hong, M. Kohne, M. Morrell, H. Wang and E. R. Weeks, *Phys. Rev. E*, 2017, **96**, 062605.
29 A. Marin, H. Lhuissier, M. Rossi and C. J. Kähler, *Phys. Rev. E*, 2018, **97**, 021102.
30 M. Souzy, I. Zuriguel and A. Marin, *Phys. Rev. E*, 2020, **101**, 060901.
31 D. Lootens, H. van Damme, Y. Hemar and P. Hebraud, *Phys. Rev. Lett.*, 2005, **95**, 268302.
32 L. C. Hsiao, S. Jamali, E. Glynos, P. F. Green, R. G. Larson and M. J. Solomon, *Phys. Rev. Lett.*, 2017, **119**, 158001.
33 C. P. Hsu, S. N. Ramakrishna, M. Zanini, N. D. Spencer and L. Isa, *Proc. Natl. Acad. Sci. U. S. A.*, 2018, **115**, 5117–5122.
34 E. Akbari Fakhrabadi, C. Bullard and M. Liberatore, *Rheol. Acta*, 2021, **60**, 251–262.
35 M. Zanini, C. P. Hsu, T. Magrini, E. Marini and L. Isa, *Colloids Surf., A*, 2017, **532**, 116–124.
36 Y. Xia and G. M. Whitesides, *Angew. Chem., Int. Ed.*, 1998, **37**, 550–575.
37 W. Thielicke and E. J. Stamhuis, *J. Open Res. Software*, 2014, **2**, e30.
38 R. Ball and J. Melrose, *Adv. Colloid Interface Sci.*, 1995, **59**, 19–30.
39 A. A. Catherall, J. R. Melrose and R. C. Ball, *J. Rheology*, 2000, **44**, 1–25.
40 D. Howell, R. P. Behringer and C. Veje, *Phys. Rev. Lett.*, 1999, **82**, 5241–5244.
41 S. Chialvo, J. Sun and S. Sundaresan, *Phys. Rev. E: Stat., Nonlinear, Soft Matter Phys.*, 2012, **85**, 021305.
42 Z. Tang, T. A. Brzinski, M. Shearer and K. E. Daniels, *Soft Matter*, 2018, **14**, 3040–3048.
43 A. L. Thomas, Z. Tang, K. E. Daniels and N. M. Vriend, *Soft Matter*, 2019, **15**, 8532–8542.
44 N. Fernandez, R. Mani, D. Rinaldi, D. Kadau, M. Mosquet, H. Lombois-Burger, J. Cayer-Barrioz, H. J. Herrmann, N. D. Spencer and L. Isa, *Phys. Rev. Lett.*, 2013, **111**, 108301.
45 C. P. Hsu, J. Mandal, S. N. Ramakrishna, N. D. Spencer and L. Isa, *Nat. Commun.*, 2021, **12**, 1477.